Journal of Alloys and Compounds 885 (2021) 160919

Contents lists available at ScienceDirect

Journal of Alloys and Compounds

journal homepage: www.elsevier.com/locate/jalcom

3D nickel diselenide architecture on nitrogen-doped carbon as a highly efficient electrode for the electrooxidation of methanol and urea

Yue Shi, Huiru Li, Dana Ao, Ying Chang, Aiju Xu, Meilin Jia*, Jingchun Jia*

College of Chemistry and Environmental Science, Inner Mongolia Key Laboratory of Green Catalysis and Inner Mongolia Collaborative Innovation Center for Water Environment Safety, Inner Mongolia Normal University, Hohhot 010022, China

ARTICLE INFO

Article history:
Received 21 April 2021
Received in revised form 14 June 2021
Accepted 19 June 2021
Available online 22 June 2021

Keywords:
Nickel selenide
Nickel diselenide
Electrooxidation
Methanol
Urea

ABSTRACT

The development of an electrocatalyst for the efficient catalysis of methanol or urea is essential for solving energy and environmental problems. This study successfully synthesizes nickel selenide and 3D nickel diselenide architectures on N-doped carbon using a NaCl-assisted method and selenization temperature regulation. The 3D architecture of the nickel diselenide with N-doped carbon obtained by selenization at 450 °C ($NiSe_2$/NC-450) is a useful electrocatalyst for the methanol oxidation reaction (MOR) and urea oxidation reaction (UOR). This $NiSe_2$/NC-450 electrode displays good catalytic activity for MOR (high peak current density of ~164.68 mA cm^{-2}, low oxidation potential of ~1.33 V at 10 mA cm^{-2}) and UOR (high peak current density of ~136.04 mA cm^{-2}, low oxidation potential of ~1.32 V at 10 mA cm^{-2}). The strong methanol and urea reaction performance of $NiSe_2$/NC-450 is attributed to the expanded electrochemically active area after selenization and the enhanced conductivity after N-doped carbon. This study provides a new way to prepare and utilize inexpensive transition metal-based materials as efficient and stable anodic oxidation electrocatalysts.

1. Introduction

With the advancement of technology and the depletion of fossil fuels, energy overuse and environmental degradation are already the most concerning global issues [1–3]. Hydrogen production by electrochemical water splitting and fuel cells are considered to be an efficient and safe clean energy device [4,5]. Numerous reports on electrochemical water splitting have found that the oxygen evolution reaction (OER) process impedes efficient hydrogen production because of its complex reaction process, slow kinetics, and large overpotential [6–8]. The methanol oxidation reaction (MOR) can be used as a replacement reaction to accelerate anodic oxidation [9]. MOR is also a key half-reaction in direct methanol fuel cells (DMFCs). Methanol exhibits high energy density, superior activity, and rich source pathways as an energy carrier [10,11]. More importantly, methanol is a common pollutant in technical water used by industrial facilities. The environmental pollution of methanol-rich wastewater is alleviated by the MOR. The use of a catalyst in the MOR is essential for achieving an optimal oxidation performance. Pt-based materials and alloys are excellent catalysts for methanol oxidation [10,12,13]. However, the high cost and low abundance of Pt hinder the commercialization of DMFCs [14]. Additionally, Pt has a low utilization rate and high toxicity during methanol oxidation [15–17]. Therefore, scientists have noted the availability of alternative transition metal anode catalysts with lower costs and better methanol oxidation performance [18]. Among the transition metal catalysts, nickel-based materials are potential catalysts due to their strong surface oxidation properties [19,20]. For example, Ni and N-doped carbon complexes were prepared by pyrolysis and used as catalysts, and exhibited a high MOR activity and prolonged stability [21]. Crystalline Ni_3B nanomaterials, with high catalytic performance, superior cycling stability, and a current density that could still be maintained at 87% after 1000 cycles, were prepared by dry powder annealing [22]. Mesoporous nickel phosphate nanotubes prepared by coprecipitation showed superior MOR activity and outstanding stability [23]. Recently, metal selenides displayed a higher electrical conductivity than sulfides and oxides because of their unique metallic properties [24,25]. Meanwhile, combining metallic selenides with carbon substrates containing heterogeneous atomic doping can reduce particles agglomeration and further improve the electrical conductivity [26,27]. Moreover, some studies have reported that selenization can improve the MOR activity (Table S1).

* Corresponding authors.
E-mail addresses: jml@imnu.edu.cn (M. Jia), jjc1983@126.com (J. Jia).

https://doi.org/10.1016/j.jallcom.2021.160919
0925-8388/

Urea is considered to be a powerful alternative energy source because of its high hydrogen content, nontoxicity, stability, and low cost [28–30]. Additionally, urea can be obtained from human and animal urine, overused fertilizers, and wastewater from urea-producing industries [31,32]. The energy conversion technologies for urea, including urea electrolysis and direct urea fuel cells (DUFCs), offer at least three advantages, namely, urea is solid at room temperature, which makes it easy to transport and store; electrocatalytic urea reduces energy consumption and indirectly promotes the production of cheap hydrogen [33,34]; and the theoretical open-circuit voltage of DUFCs (1.15 V) is lower than that of hydrogen fuel cells (1.23 V) [35,36], demonstrating its promising future. These advantages mean that urea is an ideal fuel for fuel cells. However, an excellent catalyst is required to optimize the urea oxidation reaction (UOR) performance. Relatively inexpensive nickel-based electrocatalysts, such as Ni nanowire arrays [37], nickel phosphide nanoflake arrays [38], NiCo layered double hydroxide [30], and porous ultrathin $Ni(OH)_2$ catalysts [39], have been developed as effective materials for electrocatalytic urea oxidation under alkaline conditions. There are also some selenium-based materials that exhibit excellent catalytic activity in the UOR (Table S2).

Herein, nickel selenide and nickel diselenide nanoparticles were designed and synthesized through NaCl-assisted method and selenization at different temperatures, and the 3D architecture of nickel diselenide on N-doped carbon ($NiSe_2$/NC-450) was demonstrated to be a highly reactive and reliable catalyst for MOR and UOR. The peak current density of $NiSe_2$/NC-450 reached 164.68 mA cm^{-2}, and the potential was merely 1.33 V (corresponding to 10 mA cm^{-2}) in the MOR. For urea electrolysis, the peak current density of $NiSe_2$/NC-450 reached 136.04 mA cm^{-2}, and the potential was 1.32 V (corresponding to 10 mA cm^{-2}). The excellent performance of $NiSe_2$/NC-450 as MOR and UOR electrocatalysts is attributed to the interface between the N-doped carbon and nickel diselenide. N-doped carbon as a conductive carrier can accelerate electron transport and generate more reactive sites by limiting the growth of $NiSe_2$ on the carrier. Thus, this work offers a facile, extensible, and environmentally friendly approach to prepare low-cost, highly active, and easily accessible electrocatalysts, which is valuable for further research on MOR and UOR.

2. Experimental

2.1. Catalysts synthesis

$NiCl_2$•$6H_2O$ (0.3565 g, 1.5 mM), 0.50 g of glucose, 3.51 g of NaCl, and DI (deionized) water were combined. The solution was lyophilized in a freeze dryer for 24 h. The solid product was pyrolyzed at 800 °C for 180 min in a quartz tube under an Ar atmosphere. The resulting black material was treated with DI water to eliminate NaCl and then dried under vacuum. Subsequently, the dried product was mixed with dicyandiamide and heated at 800 °C for 180 min under an Ar atmosphere. Finally, the synthesized product was burned in air at 300 °C for 2 h. The synthesized precursor was labeled Ni/NC.

Nickel nanoparticles as obtained above and selenium powder (volume scale = 1:5) were placed into separate porcelain boats in a tube furnace. A selenium powder-filled porcelain boat was placed upstream by heating for 180 min at 450 °C in an Ar atmosphere, yielding $NiSe_2$/NC-450. Finally, $NiSe_2$/NC-350, $NiSe_2$/NC-550, NiSe/NC-650, and NiSe/NC-750 were obtained by adopting the same reaction parameters, only changing the temperature of selenization. $NiSe_2$/NC-450-no template (without NaCl) and $NiSe_2$/C-450 (without N) were synthesized using the same preparation method and used to compare the effects of NaCl and N doping.

2.2. Physical characterizations

Powder X-ray diffraction (XRD) measurements were conducted using a German Bruker D8 Advance instrument. X-ray photoelectron spectroscopy (XPS, ESCALAB 250Xi) was used to analyze the electronic structures of the elements in the sample. Scanning electron microscopy (SEM, Japan Hitachi cold field emission S4800) and field-emission transmission electron microscopy (FE-TEM, Tecnai G2 F20) were used to study the morphology of the catalyst. X-ray spectroscopy (EDS) analysis and elemental mapping were conducted using an FEI Tecnai G2 F20 instrument. Nitrogen adsorption-desorption measurements were measured to determine the Brunauer-Emmett-Teller (BET) specific surface areas of samples using a Micromeritics ASAP 2020 system.

2.3. Electrochemical characterizations

Electrochemical data was obtained using a CHI760E electrochemical workstation at room temperature. The MOR and UOR measurements were evaluated in a conventional three-electrode configuration using carbon paper as the working electrode (0.5 × 0.5 cm^2), platinum wire as the counter electrode, and an Hg/HgO electrode as the reference electrode. A catalyst slurry for the electrochemical experiment was prepared by uniformly combining 2 mg of the catalyst sample with 400 μL of a solution containing Nafion, DI water, and ethanol. Then, the carbon paper was uniformly coated with 25 μL of slurry and dried under infrared light. The measured MOR and UOR potentials were expressed as reversible hydrogen electrodes (that is, vs. RHE). All experimental data showed that no IR correction was performed. Linear sweep voltammetry (LSV) and cyclic voltammetry (CV) were employed to test the catalyst performance from 1.1 to 1.7 V. Electrochemical impedance spectroscopy (EIS) was performed at 1.35 V with a frequency range of 0.01–100 kHz. All electrochemical experiments were performed using an electrolyte consisting of KOH and KOH containing methanol (or urea).

3. Results and discussion

3.1. Physical characterizations

In the synthesis process, nickel precursors were prepared by lyophilization and pyrolysis using NaCl as a template. Then, dicyandiamine was added to the precursor as a nitrogen source and selenized at different temperatures to obtain nickel selenide and nickel diselenide. Finally, the obtained catalysts were used for MOR and UOR. Fig. 1a shows the catalyst preparation process.

The morphology of the catalyst was characterized by SEM. First, the morphology of the catalyst without NaCl in the sample revealed that a large number of irregular carbon blocks were generated (Fig. S1a–c). However, after the addition of NaCl, all samples could generate nanosheet structures, which proved that NaCl played a decisive role in the generation of the nanosheet structure (Fig. 1b–d and Fig. S1d-l). The morphologies of $NiSe_2$/NC-350, $NiSe_2$/NC-450, and $NiSe_2$/NC-550 were similar to those of Ni/NC, indicating that the selenization process did not destroy the catalyst morphology. Ni/NC, $NiSe_2$/NC-350, $NiSe_2$/NC-450, and $NiSe_2$/NC-550 exhibited some 3D columnar structures growing on the nanosheet layers. The 3D columnar structure originates from the carbon catalyzing the growth of Ni under high-temperature conditions. The 3D architecture of $NiSe_2$/NC-450 was more tightly arranged that of $NiSe_2$/NC-350 and $NiSe_2$/NC-550. The TEM image (Fig. 1e) further confirmed the presence of the 3D architecture on the sheet carbon skeleton substrate. Additionally, the HR-TEM image (Fig. 1f) shows that the sample surface was covered by uniform stripes with a spacing of 0.298 nm, demonstrating the (200) lattice surface of $NiSe_2$/NC-450. The

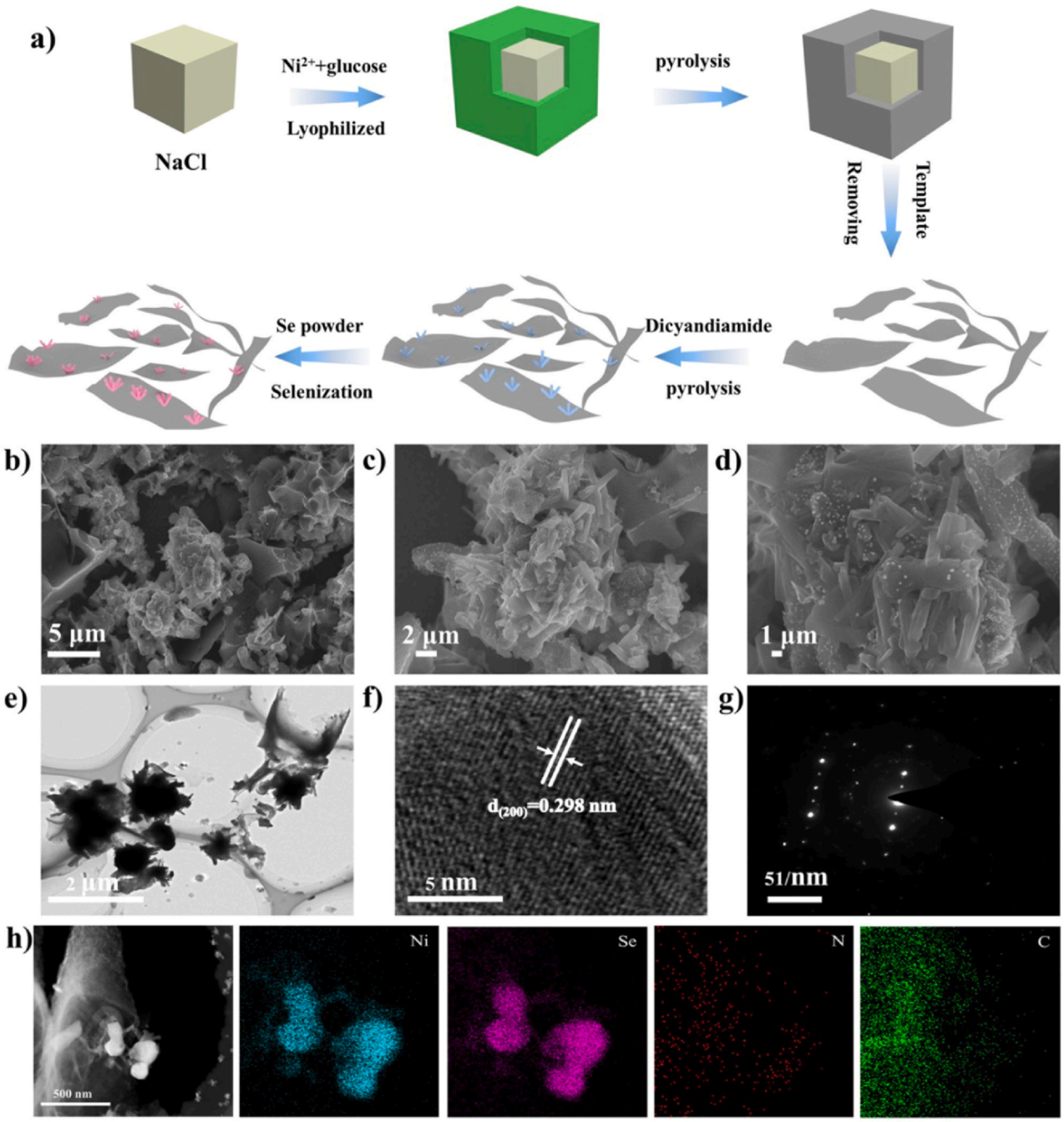

Fig. 1. a) Synthesis diagrams of $NiSe_2$/NC and NiSe/NC; (b–d) SEM images of $NiSe_2$/NC-450 at different magnifications; (e) TEM images of $NiSe_2$/NC-450; (f) HR-TEM images of $NiSe_2$/NC-450; (g) SAED images of $NiSe_2$/NC-450; and (h) elemental mapping of $NiSe_2$/NC-450.

selected area electron diffraction (SAED) pattern of $NiSe_2$/NC-450 (Fig. 1g) revealed that $NiSe_2$/NC-450 displays a high degree of crystallinity. The relationship between the content of NiSe and the carrier was observed from the EDS spectra of $NiSe_2$/NC-350, $NiSe_2$/NC-450, and $NiSe_2$/NC-550. The four elements, namely Ni, Se, N, and C, were obtained from the EDS spectra of $NiSe_2$/NC-350, $NiSe_2$/NC-450, and $NiSe_2$/NC-550. It is noteworthy that the contents of Ni and Se in $NiSe_2$/NC-450 were significantly higher than those in $NiSe_2$/NC-350 and $NiSe_2$/NC-550, which may be the reason for the better MOR and UOR performance of $NiSe_2$/NC-450 (Fig. S2 and Table S3). Moreover, the elemental mapping of $NiSe_2$/NC-450 demonstrates that Ni, Se, N, and C were distinctly present and uniformly distributed in the composite (Fig. 1h).

The crystalline structures of Ni/NC, nickel diselenide, and nickel selenide were characterized by XRD (Fig. 2a and Fig. S3). Nickel diselenide was synthesized at temperatures ranging from 350 to 550 °C, while nickel selenide was synthesized at 650 °C and 750 °C. The characteristic peaks of nickel diselenide at 29.945, 33.579, 36.893, 50.737, and 55.519 correspond to the (200), (210), (211), (311), and (023) crystal planes, respectively (JCPDS card no. 88-1711). The characteristic peaks of nickel selenide at 32.848, 44.373, 49.785, 59.606, and 68.872 correspond to the (101), (102), (110), (103), and (202) planes, respectively (JCPDS card no. 75-0610). Meanwhile, the crystalline phase of the catalyst changed from a cubic crystalline phase ($NiSe_2$) to a hexagonal crystalline phase (NiSe) as the temperature increased, indicating that the annealing temperature

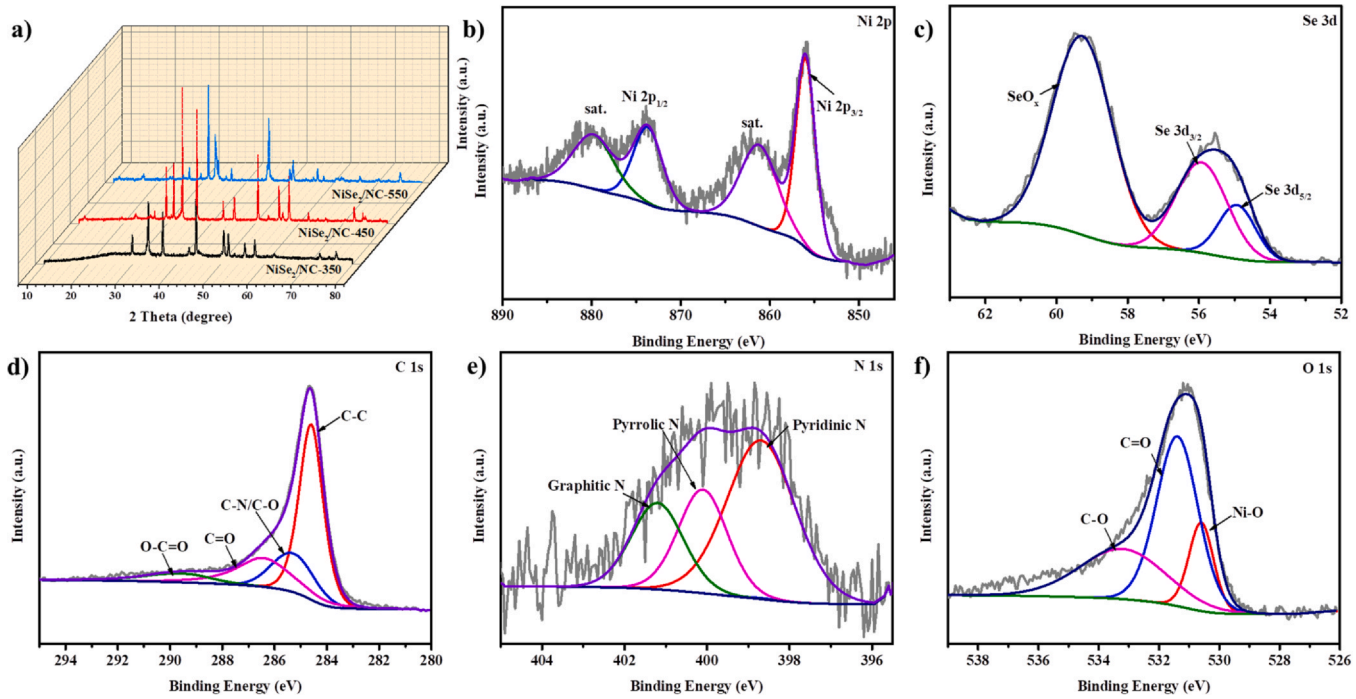

Fig. 2. (a) XRD patterns of $NiSe_2$/NC-350, $NiSe_2$/NC-450, and $NiSe_2$/NC-550; (b) XPS spectrum tests of (b) Ni 2p, (c) Se 3d, (d) C 1s, (e) N 1s; and (f) O 1s of $NiSe_2$/NC-450.

significantly impacted the crystalline phase of the catalyst. The crystalline phase of nickel selenide is related to the atomic ratio between nickel and selenium. When selenization was conducted at 350–550 °C, a cubic crystalline phase ($NiSe_2$) was formed owing to the relatively stable selenium. However, at higher temperatures (650 °C and 750 °C), a hexagonal crystalline phase (NiSe) was obtained because of the evaporation of selenium, resulting in a decrease in the selenium content [40].

Subsequently, the chemical components of $NiSe_2$/NC-450 were determined using XPS. In the XPS spectra of the $NiSe_2$/NC-450 used for surface measurements, Ni, O, N, C, and Se peaks were detected, suggesting that these elements were present (Fig. S4). Fig. 2b displays the Ni 2p profile, clearly revealing the two primary peaks at 855.98 eV and 873.69 eV associated with Ni^{2+} in $NiSe_2$/NC-450 [26,41]. There are also peaks at approximately 861.19 eV and 879.80 eV derived from the satellite structure. Peaks at 55.5 and 59.28 eV were detected in Fig. 2c, suggesting the existence of Ni—Se bonds and oxide species of Se [42–44]. In the C 1s spectrum (Fig. 2d), the four main constituents were C—C (284.60 eV), C—N/C—O (285.30 eV), C═O (286.40 eV), and O—C═O (289.46 eV) [45,46]. The N 1s spectrum (Fig. 2e) demonstrated the presence of pyridinic-N (398.69 eV), pyrrolic-N (400.10 eV), and graphitic-N (401.20 eV) [47]. Ni—O (530.60 eV), C═O (531.39 eV), and C—O (532.21 eV) bonds were detected in the O 1s spectra (Fig. 2f) [48,49].

The surface area of the samples was measured using a nitrogen adsorption-desorption isotherm (Fig. S5). The surface areas of the $NiSe_2$/NC-450-no template, Ni/NC, and $NiSe_2$/NC-450 obtained by the BET method were 42.18, 95.47, and 108.14 $m^2\ g^{-1}$, respectively. The significantly larger surface areas of Ni/NC and $NiSe_2$/NC-450, as compared to the $NiSe_2$/NC-450-no template, were attributed to the addition of NaCl as a template. The slight increase in the surface area of $NiSe_2$/NC-450, as compared to Ni/NC, may be due to the collapse of the carbon substrate by the combination of Ni nanoparticles and Se powder under the effect of selenization.

3.2. Electrochemical characterizations

3.2.1. Electrochemical behavior of nickel-based catalysts in a pure KOH solution

To investigate the reactive behavior of the previously fabricated nickel-based catalysts, bare carbon paper substrate and nickel-based catalysts were tested in a pure KOH solution (Fig. 3a). Compared with bare carbon paper, all nickel-based catalysts exhibited redox peaks, indicating the existence of redox reactions between Ni^{2+} and Ni^{3+}. The electrochemical active surface area (ECSA) is regarded as a useful reference to gain a deeper understanding of the activity of nickel-based catalysts. ECSA can be gauged by calculating the double-layer capacitance (C_{dl}), as there is a positive correlation between them [34,50]. The C_{dl} was identified from different catalysts in the non-Faraday region of the CV plots (Fig. S6). The C_{dl} of $NiSe_2$/NC-450 (Fig. 3b) was higher than that of the previously prepared nickel-containing catalysts. Additionally, CV plots of all nickel-based catalysts in pure KOH from 5 to 80 mV s^{-1} were constructed (Fig. 3c and Fig. S7a–e). The anodic peak current density (Ip) and peak potential changed with an increasing scanning speed. The peak offset emanates from the limitation of the reaction kinetics [51]. Fig. 3d and Fig. S7f–j further investigate the relationship between the Ip and the square root of the scan rate ($v^{1/2}$), and a linear relationship between Ip and $v^{1/2}$ was identified [52]. This indicates that the redox process was mainly regulated by diffusion. Compared with the other prepared catalysts, $NiSe_2$/NC-450 exhibited the largest electrochemically active area, which can be ascribed to its unique 3D architecture.

3.2.2. Electrocatalytical activity for MOR

The MOR behaviors of the catalysts were evaluated using different test methods. Fig. 4a presents the comparative CVs of $NiSe_2$/NC-450 before and after adding it to 0.5 M MeOH in a 1 M KOH electrolyte solution. After adding methanol, the peak current density

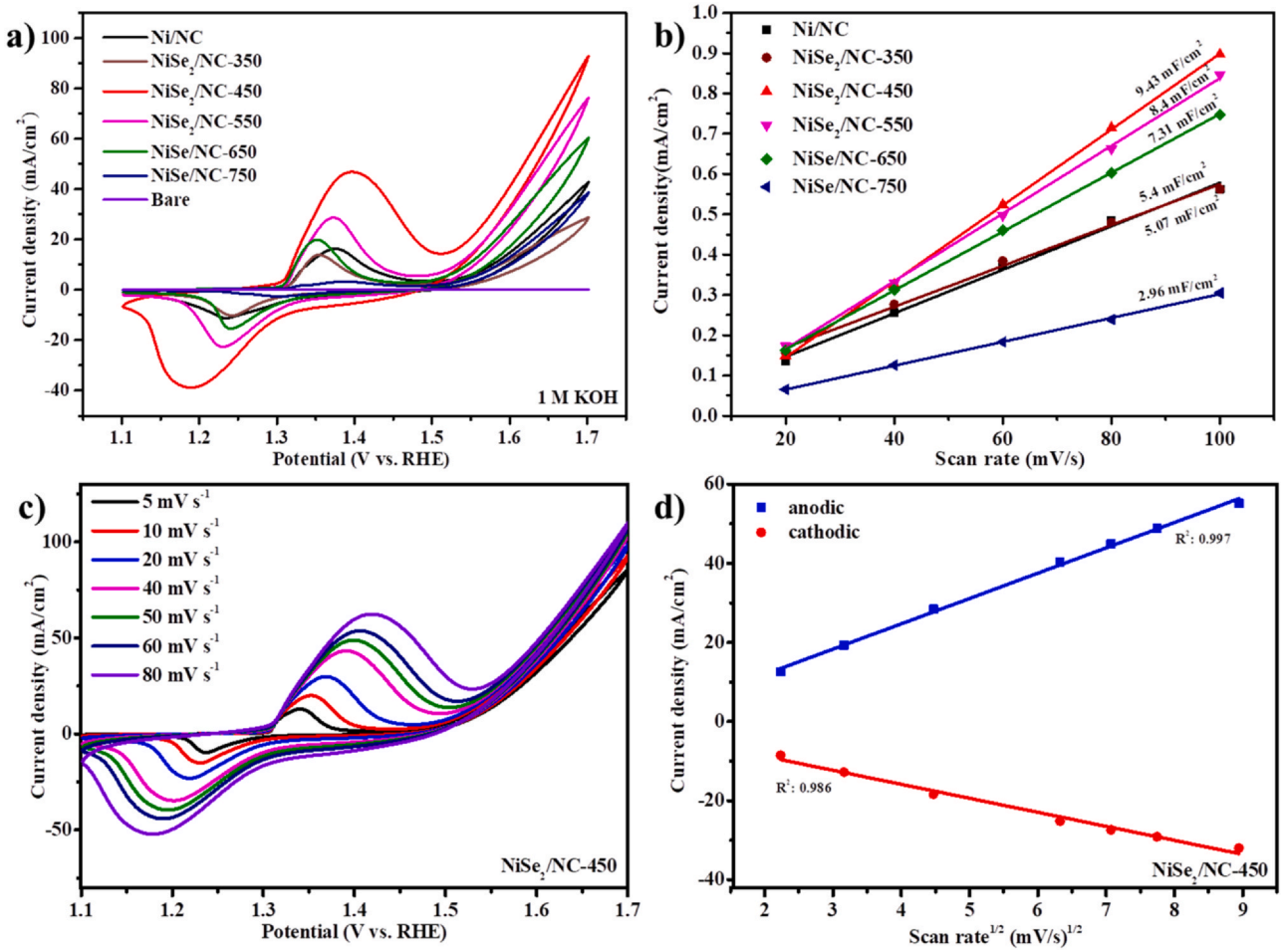

Fig. 3. Electrochemical performance in a 1 M KOH solution. (a) Comparison of CV plots for the bare carbon paper substrate and nickel-based catalysts (sweep speed: 50 mVs^{-1}); (b) the C_{dl} of nickel-based catalysts with the potential at 1.15 V; (c) CV plots of $NiSe_2$/NC-450 from 5 to 80 mV s^{-1}; and (d) linear fitting of the anodic and cathodic peak current densities with the square roots of the scan rate in the scan rate range (5–80 mV s^{-1}) for $NiSe_2$/NC-450.

of $NiSe_2$/NC-450 reached 167.44 mA cm^{-2}. The LSV measurements of $NiSe_2$/NC-450 showed that the potential decreased significantly after the addition of methanol (Fig. S8a). To reach 10 mA cm^{-2}, only 1.33 V was required. These measurements indicate that $NiSe_2$/NC-450 exhibited a remarkable methanol oxidation performance. The selenization temperature of the precursors had a significant effect on the MOR. The CVs of Ni/NC, $NiSe_2$/NC-350, $NiSe_2$/NC-450, $NiSe_2$/NC-550, NiSe/NC-650, and NiSe/NC-750 (Fig. 4b) showed electrocatalytic activity in the MOR. Apparently, $NiSe_2$/NC-450 shows higher MOR activity than other previously prepared nickel-based materials, and this may be because the catalyst acquires ample active sites during selenization at 450 °C. However, it should be noted that $NiSe_2$/NC-350 and NiSe/NC-750 had similar current densities to Ni/NC, indicating that lower or higher selenization temperatures can lead to the destruction of the catalyst morphology and thus affect the catalytic performance. Additionally, LSV testing of all catalysts demonstrated that $NiSe_2$/NC-450 had the lowest potential (Fig. S8b). Generally, the active substrate of nickel-based catalysts in alkaline electrocatalytic methanol is NiOOH, which originates and oxidizes methanol, as shown below [50,53].

$$Ni(OH)_2 + OH^- \rightarrow NiOOH + H_2O + e^- \quad (1)$$

$$NiOOH + CH_3OH + 1.25O_2 \rightarrow Ni(OH)_2 + CO_2 + 1.5H_2O \quad (2)$$

To determine the charge transfer capability and electrocatalytic kinetics at the electrode interface, EIS tests were performed at 1.35 V, as shown in Fig. 4c. The spectra of all samples showed a single semicircle. The semicircular radius of $NiSe_2$/NC-450 was clearly smaller than that of Ni/NC and the other catalysts synthesized at different selenization temperatures, indicating that $NiSe_2$/NC-450 had a smaller charge transfer resistance and faster electrocatalytic kinetics. NiSe/NC-750 prepared by selenization at 750 °C had the largest semicircle radius, implying that high temperature is unfavorable for the charge transfer and catalytic kinetic properties of nickel selenide nanoparticles.

Durability is an essential indicator for determining the lifetime of electrocatalysts in practical applications. The durability of the synthesized catalysts was examined for 10,000 s using a chronoamperometry test at 1.5 V (Fig. 4d). There was a sharp drop in the current density at all electrodes in the first few seconds. This drop was probably due to the active sites being occupied by the accumulated strongly adsorbed intermediate species, resulting in active site poisoning. Subsequently, the current gradually approached a steady state. After 10,000 s, the residual current density of $NiSe_2$/NC-450 (74.36 mA cm^{-2}) was 2.08, 1.53, 1.13, 1.27, and 2.85 times that of Ni/NC (35.672 mA cm^{-2}), $NiSe_2$/NC-350 (48.52 mA cm^{-2}), $NiSe_2$/NC-550 (65.8 mA cm^{-2}), NiSe/NC-650 (58.48 mA cm^{-2}), and NiSe/NC-750 (26.12 mA cm^{-2}), respectively. $NiSe_2$/NC-450 was examined with TEM after the stability test, revealing that the electrocatalyst maintained the sheet carbon skeleton structure (Fig. S9). These results indicate that $NiSe_2$/NC-450 exhibited high stability in the MOR.

By selenizing the precursors at different temperatures, it was found that selenization at 450 °C resulted in a better methanol oxidation performance. Subsequently, the impact of the template and N

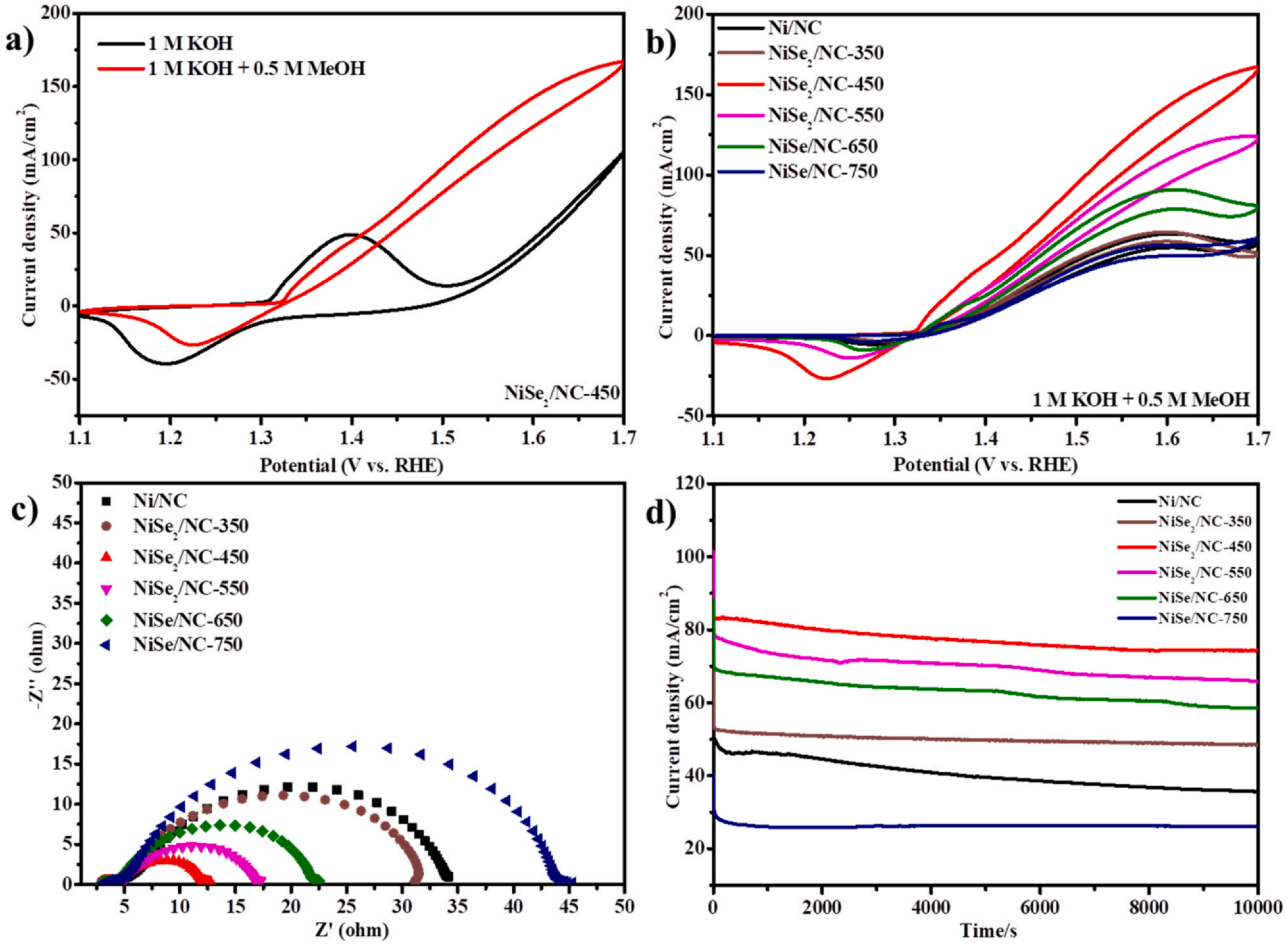

Fig. 4. (a) CVs of $NiSe_2$/NC-450 in different electrolytes (sweep speed: 50 mVs^{-1}); (b) CVs of Ni/NC, $NiSe_2$/NC-350, $NiSe_2$/NC-450, $NiSe_2$/NC-550, NiSe/NC-650, and NiSe/NC-750 in 1 M KOH containing 0.5 M MeOH (sweep speed: 50 mVs^{-1}); (c) EIS of Ni/NC, $NiSe_2$/NC-350, $NiSe_2$/NC-450, $NiSe_2$/NC-550, NiSe/NC-650, and NiSe/NC-750 in 1 M KOH containing 0.5 M MeOH at 1.35 V; and (d) chronoamperometry curves of Ni/NC, $NiSe_2$/NC-350, $NiSe_2$/NC-450, $NiSe_2$/NC-550, NiSe/NC-650, and NiSe/NC-750 in 1 M KOH containing 0.5 M MeOH at 1.5 V.

doping on the MOR performance at the optimal selenization temperature was measured. From the results of the LSV and CV tests, $NiSe_2$/NC-450 had a lower onset potential and higher current density than the $NiSe_2$/C-450 and $NiSe_2$/NC-450-no template (Fig. S10a-b). Meanwhile, the EIS test results show that $NiSe_2$/NC-450 had the smallest semicircular radius, while the $NiSe_2$/NC-450-no template had a larger semicircle radius (Fig. S10c). The better electrocatalytic activity of $NiSe_2$/NC-450, by comparing the MOR performance of the electrocatalyst at a selenization temperature of 450 °C, indicated that the N doping promotes electron transfer and increases the surface area after template addition, preventing particles agglomeration.

3.2.3. Electrocatalytical activity for UOR

The catalytic behavior of different samples in the UOR was evaluated. Fig. 5a shows the CV curves of $NiSe_2$/NC-450 before and after the addition of urea. The current density increased significantly after adding urea and the oxidation peak current density of $NiSe_2$/NC-450 reached 136.04 mA cm^{-2}. The LSV test was further used to determine the effect of urea addition on the potential of $NiSe_2$/NC-450 (Fig. S11a). $NiSe_2$/NC-450 demonstrated excellent UOR electrooxidation activity, requiring only 1.32 V of potential to achieve 10 mA cm^{-2}. The performance of the present work with recently reported nickel-based catalysts is summarized in Fig. S11c, showing that $NiSe_2$/NC-450 has a low potential value [28,38,54–59]. The increased UOR activity of $NiSe_2$/NC-450 may be due to the presence of additional reactive sites exposed in the unique configuration. Furthermore, the urea oxidation properties of $NiSe_2$/NC-450, Ni/NC, and selenide obtained by selenization at different temperatures were compared. Fig. 5b illustrates the higher UOR activity of $NiSe_2$/NC-450 as compared to that of Ni/NC and the other prepared selenides. Meanwhile, LSV tests were performed on all catalysts in a 1 M KOH with 0.5 M urea solution (Fig. S11b). Compared with the other catalysts, $NiSe_2$/NC-450 still had the lowest potential, demonstrating that $NiSe_2$/NC-450 has faster oxidation kinetics for urea. All test results showed that $NiSe_2$/NC-450 exhibited the best catalytic activity in the UOR process. Moreover, $NiSe_2$/NC-350 exhibited electrocatalytic activity similar to that of Ni/NC during urea oxidation, while NiSe/NC-750 was considerably inferior to Ni/NC. This experimental phenomenon, as in the case of methanol oxidation, indicates that selenization at both high and low temperatures is not favorable for enhancing the electrooxidation activity of the materials. It is worth noting that NiOOH is also an active species in the UOR process under alkaline conditions. The electrochemical oxidation of urea is described below [28,58].

$$6Ni(OH)_2 + 6OH^- \rightarrow 6NiOOH + 6H_2O + 6e^- \quad (3)$$

$$6NiOOH + CO(NH_2)_2 + H_2O \rightarrow 6Ni(OH)_2 + CO_2 + N_2 \quad (4)$$

To further study the effect of the selenization temperature on conductivity during urea electrolysis, EIS experiments were conducted at 1.35 V (Fig. 5c). The test results showed that $NiSe_2$/NC-450 has the smallest semicircle radius, indicating that $NiSe_2$/NC-450 has

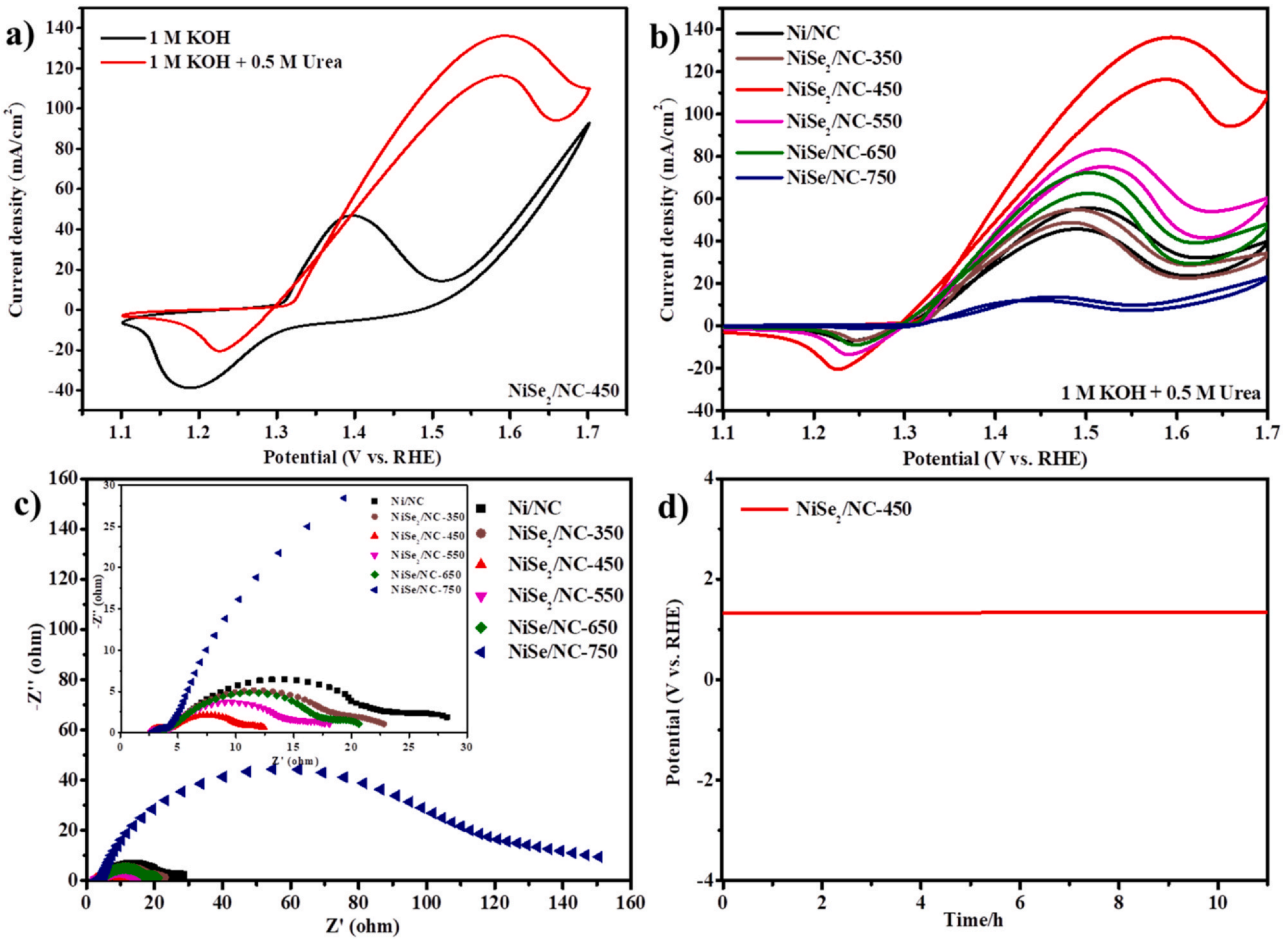

Fig. 5. (a) CVs of $NiSe_2$/NC-450 in different electrolytes (sweep speed: 50 mV s^{-1}); (b) CVs of Ni/NC, $NiSe_2$/NC-350, $NiSe_2$/NC-450, $NiSe_2$/NC-550, NiSe/NC-650, and NiSe/NC-750 in 1 M KOH containing 0.5 M Urea (sweep speed: 50 mV s^{-1}); (c) EIS of Ni/NC, $NiSe_2$/NC-350, $NiSe_2$/NC-450, $NiSe_2$/NC-550, NiSe/NC-650, and NiSe/NC-750 in 1 M KOH containing 0.5 M urea at 1.35 V; and (d) chronopotentiometry curve of $NiSe_2$/NC-450 in 1 M KOH containing 0.5 M urea at 10 mA cm^{-2}.

a high conductivity and charge transfer rate during urea oxidation. In contrast, NiSe/NC-750 has a larger semicircle radius than Ni/NC, implying that selenization at high temperatures affects the kinetic behavior of the electrocatalyst.

To assess the durability of $NiSe_2$/NC-450 in the urea oxidation process, chronopotentiometry curve and multistep chronopotentiometric test were obtained. The chronopotentiometry curve of $NiSe_2$/NC-450 for the electrooxidation of urea was obtained at 10 mA cm^{-2}. Fig. 5d shows that the potential of $NiSe_2$/NC-450 essentially remained constant for 10 h, indicating that $NiSe_2$/NC-450 shows good durability in long-term catalytic urea oxidation. The TEM analysis demonstrated that $NiSe_2$/NC-450 also maintains the carbon skeleton structure after the stability test, demonstrating the remarkable stability of the electrocatalyst (Fig. S12). Subsequently, the multistep chronopotentiometric bight of $NiSe_2$/NC-450 was investigated in a solution containing 1 M KOH and 0.5 M urea. The current density gradually increased from 10 to 90 mA cm^{-2} with an increase of 10 mA cm^{-2} every 200 s (Fig. S13). The potential of each stage remained stable for its corresponding 200 s, indicating that $NiSe_2$/NC-450 has outstanding mechanical strength, mass transportation, and electroconductive properties [58,60,61].

The effects of N doping and template on the UOR performance were measured by LSV, CV, and EIS tests (Fig. S14). All tests showed that $NiSe_2$/NC-450 has a superior urea oxidation activity as compared to the undoped N and no-template electrocatalysts, demonstrating that the doping of N and the introduction of the template favor the oxidation of urea. This result is consistent with that of the methanol oxidation.

The remarkable electrochemical activity of the $NiSe_2$/NC-450 3D architecture for methanol and urea electrooxidation is largely driven by the following: (1) The unique 3D architecture provides good stability and allows for rapid access of electrolyte solutions to the surface for efficient oxidation of methanol and urea. (2) N-doped carbon enhanced the carbon matrix conductivity and accelerated electron transport at the catalytic interface. (3) An appropriate selenization temperature facilitates the expansion of the electrochemically active region and the generation of additional positive reaction sites. The simple preparation, cost-effectiveness, and efficient electrochemical performance of $NiSe_2$/NC-450 makes it a promising competitive electrocatalyst for practical methanol and urea anodic oxidation.

4. Conclusions

In summary, the nickel-based catalysts were successfully prepared using a simple and economical salt template pyrolysis and selenization. Compared to the Ni/NC and the catalysts obtained by selenization at different temperatures, $NiSe_2$/NC-450 is a more effective electrocatalyst in alkaline methanol and urea electrolysis. The enhanced electrochemical characteristics of $NiSe_2$/NC-450 are mainly due to its distinctive 3D architecture, large electrochemical reaction area, and high electrical conductivity. Therefore, the excellent methanol and urea oxidation performance of $NiSe_2$/NC-450 makes it a promising anode material.

CRediT authorship contribution statement

Jingchun Jia designed experiments. Yue Shi, Huiru Li and Dana Ao performed experiments and characterizations. Jingchun Jia, Ying Chang, Aiju Xu and Meilin Jia wrote and revised the manuscript. All the authors discussed the experiments, results and manuscript.

Declaration of Competing Interest

The authors declare that they have no known competing financial interests or personal relationships that could have appeared to influence the work reported in this paper.

Acknowledgments

We acknowledge the Collaborative Innovation Cultivating Center for Water Environment Security of Inner Mongolia Autonomous Region China (XTCX003), Science and Technology Program of Inner Mongolia Autonomous Region, China (Grant No. 2020GG0010), Inner Mongolia Normal University Graduate Student's Research & Innovation Fund (No. CXJJS20107), and the Research Foundation for Advanced Talents of Inner Mongolia Normal University (No. 2018YJRC001, and 2018YJRC012) for funding this study.

Appendix A. Supporting information

Supplementary data associated with this article can be found in the online version at doi:10.1016/j.jallcom.2021.160919.

References

[1] T. Liu, P. Li, N. Yao, G. Cheng, S. Chen, W. Luo, Y. Yin, CoP-doped MOF-based electrocatalyst for pH-universal hydrogen evolution reaction, Angew. Chem. Int. Ed. 58 (2019) 4679–4684.
[2] B. Zhang, S. Wang, Z. Ma, Y. Qiu, Ni^0-rich Ni/NiO nanocrystals for efficient water-to-hydrogen conversion via urea electro-oxidation, Appl. Surf. Sci. 496 (2019) 143710.
[3] S.F. Hung, Y.Y. Hsu, C.J. Chang, C.S. Hsu, N.T. Suen, T.S. Chan, H.M. Chen, Unraveling geometrical site confinement in highly efficient iron-doped electrocatalysts toward oxygen evolution reaction, Adv. Energy Mater. 8 (2018) 1701686.
[4] Y. Teng, X.D. Wang, J.F. Liao, W.G. Li, H.Y. Chen, Y.J. Dong, D.B. Kuang, Atomically thin defect-rich Fe-Mn-O hybrid nanosheets as high efficient electrocatalyst for water oxidation, Adv. Funct. Mater. 28 (2018) 1802463.
[5] N. Radenahmad, A. Afif, P.I. Petra, S.M.H. Rahman, S.G. Eriksson, A.K. Azad, Proton-conducting electrolytes for direct methanol and direct urea fuel cells-a state-of-the-art review, Renew. Sustain. Energy Rev. 57 (2016) 1347–1358.
[6] J. Wang, R. Kong, A.M. Asiri, X. Sun, Replacing oxygen evolution with hydrazine oxidation at the anode for energy-saving electrolytic hydrogen production, ChemElectroChem 4 (2017) 481–484.
[7] D. Wu, Y. Wei, X. Ren, X. Ji, Y. Liu, X. Guo, Z. Liu, A.M. Asiri, Q. Wei, X. Sun, Co$(OH)_2$ nanoparticle-encapsulating conductive nanowires array: room-temperature electrochemical preparation for high-performance water oxidation electrocatalysis, Adv. Mater. 30 (2018) 1705366.
[8] C. Meng, Y. Cao, Y. Luo, F. Zhang, Q. Kong, A.A. Alshehri, K.A. Alzahrani, T. Li, Q. Liu, X. Sun, A Ni-MOF nanosheet array for efficient oxygen evolution electrocatalysis in alkaline media, Inorg. Chem. Front. 8 (2021) 3007–3011.
[9] K. Xiang, D. Wu, X. Deng, M. Li, S. Chen, P. Hao, X. Guo, J.L. Luo, X.Z. Fu, Boosting H_2 generation coupled with selective oxidation of methanol into value-added chemical over cobalt hydroxide@hydroxysulfide nanosheets electrocatalysts, Adv. Funct. Mater. 30 (2020) 1909610.
[10] F. Zhao, J. Ye, Q. Yuan, X. Yang, Z. Zhou, Realizing a CO-free pathway and enhanced durability in highly dispersed Cu-doped PtBi nanoalloys towards methanol full electrooxidation, J. Mater. Chem. A 8 (2020) 11564–11572.
[11] B. Ruiz-Camacho, A. Medina-Ramírez, M. Villicaña Aguilera, J.I. Minchaca-Mojica, Pt supported on mesoporous material for methanol and ethanol oxidation in alkaline medium, Int. J. Hydrogen Energy 44 (2019) 12365–12373.
[12] H. Liu, J. Qin, S. Zhao, Z. Gao, Q. Fu, Y. Song, Two-dimensional circular platinum nanodendrites toward efficient oxygen reduction reaction and methanol oxidation reaction, Electrochem. Commun. 98 (2019) 53–57.
[13] J. Xie, Q. Zhang, L. Gu, S. Xu, P. Wang, J. Liu, Y. Ding, Y.F. Yao, C. Nan, M. Zhao, Y. You, Z. Zou, Ruthenium-platinum core-shell nanocatalysts with substantially enhanced activity and durability towards methanol oxidation, Nano Energy 21 (2016) 247–257.
[14] T. Radhakrishnan, N. Sandhyarani, Pt-Ag nanostructured 3D architectures: a tunable catalyst for methanol oxidation reaction, Electrochim. Acta 298 (2019) 835–843.
[15] M.G. Hosseini, R. Mahmoodi, V. Daneshvari-Esfahlan, Ni@Pd core-shell nanostructure supported on multi-walled carbon nanotubes as efficient anode nanocatalysts for direct methanol fuel cells with membrane electrode assembly prepared by catalyst coated membrane method, Energy 161 (2018) 1074–1084.
[16] H. Mao, Z. Cao, X. Guo, M. Liu, D. Sun, Z. Sun, H. Ge, Y. Zhang, X.M. Song, Enhanced electrocatalytic performance for the oxidation of methanol by hierarchical NiS/$Ni(OH)_2$@polypyrrole/graphene oxide nanosheets, Appl. Surf. Sci. 471 (2019) 355–367.
[17] W. Ma, J. Wu, C. Shen, H. Tang, M. Pan, Nickel phthalocyanine-tetrasulfonic acid as a promoter of methanol electro-oxidation on Pt/C catalyst, J. Appl. Electrochem. 38 (2008) 875–879.
[18] A.R. Jadhav, H.A. Bandal, A.A. Chaugule, H. Kim, Diethylenetriamine assisted synthesis of mesoporous Co and Ni-Co spinel oxides as an electrocatalysts for methanol and water oxidation, Electrochim. Acta 240 (2017) 277–287.
[19] A. Yuda, A. Ashok, A. Kumar, A comprehensive and critical review on recent progress in anode catalyst for methanol oxidation reaction, Catal. Rev. (2020) 1–103.
[20] W. Yang, X. Yang, J. Jia, C. Hou, H. Gao, Y. Mao, C. Wang, J. Lin, X. Luo, Oxygen vacancies confined in ultrathin nickel oxide nanosheets for enhanced electrocatalytic methanol oxidation, Appl. Catal. B Environ. 244 (2019) 1096–1102.
[21] N. Wu, M. Zhai, F. Chen, X. Zhang, R. Guo, T. Hu, M. Ma, Nickel nanocrystal/nitrogen-doped carbon composites as efficient and carbon monoxide-resistant electrocatalysts for methanol oxidation reactions, Nanoscale 12 (2020) 21687–21694.
[22] J. Li, F. Luo, Q. Zhao, L. Xiao, J. Yang, W. Liu, D. Xiao, Crystalline nickel boride nanoparticle agglomerates for enhanced electrocatalytic methanol oxidation, Int. J. Hydrogen Energy 44 (2019) 23074–23080.
[23] X. Song, Q. Sun, L. Gao, W. Chen, Y. Wu, Y. Li, L. Mao, J.H. Yang, Nickel phosphate as advanced promising electrochemical catalyst for the electro-oxidation of methanol, Int. J. Hydrogen Energy 43 (2018) 12091–12102.
[24] W. Hou, J. He, B. Yu, Y. Lu, W. Zhang, Y. Chen, One-pot synthesis of graphene-wrapped $NiSe_2$-$Ni_{0.85}Se$ hollow microspheres as superior and stable electrocatalyst for hydrogen evolution reaction, Electrochim. Acta 291 (2018) 242–248.
[25] D. Yang, Y. Liu, B. Wang, J. He, Y. Chen, $NiSe_2$ nanocrystals anchored graphene nanosheets as highly efficient and stable electrocatalyst for hydrogen evolution reaction in alkaline medium, J. Alloy. Compd. 792 (2019) 789–796.
[26] W. Li, B. Yu, Y. Hu, X. Wang, D. Yang, Y. Chen, Core-shell structure of $NiSe_2$ nanoparticles@nitrogen-doped graphene for hydrogen evolution reaction in both acidic and alkaline media, ACS Sustain. Chem. Eng. 7 (2019) 4351–4359.
[27] J. Zhou, Z. Wang, D. Yang, F. Qi, X. Hao, W. Zhang, Y. Chen, $NiSe_2$-anchored N,S-doped graphene/Ni foam as a free-standing bifunctional electrocatalyst for efficient water splitting, Nanoscale 12 (2020) 9866–9872.
[28] H. Yang, M. Yuan, Z. Sun, D. Wang, L. Lin, H. Li, G. Sun, In situ construction of a Mn^{2+}-doped Ni_3S_2 electrode with highly enhanced urea oxidation reaction performance, ACS Sustain. Chem. Eng. 8 (2020) 8348–8355.
[29] D. Wang, S.H. Vijapur, Y. Wang, G.G. Botte, $NiCo_2O_4$ nanosheets grown on current collectors as binder-free electrodes for hydrogen production via urea electrolysis, Int. J. Hydrogen Energy 42 (2017) 3987–3993.
[30] M. Zeng, J. Wu, Z. Li, H. Wu, J. Wang, H. Wang, L. He, X. Yang, Interlayer effect in NiCo layered double hydroxide for promoted electrocatalytic urea oxidation, ACS Sustain. Chem. Eng. 7 (2019) 4777–4783.
[31] B. Zhu, Z. Liang, R. Zou, Designing advanced catalysts for energy conversion based on urea oxidation reaction, Small 16 (2020) 1906133.
[32] S. Hu, S. Wang, C. Feng, H. Wu, J. Zhang, H. Mei, Novel MOF-derived nickel nitride as high-performance bifunctional electrocatalysts for hydrogen evolution and urea oxidation, ACS Sustain. Chem. Eng. 8 (2020) 7414–7422.
[33] X. Xu, P. Du, T. Guo, B. Zhao, H. Wang, M. Huang, In situ grown Ni phosphate@$Ni_{12}P_5$ nanorod arrays as a unique core-shell architecture: competitive bifunctional electrocatalysts for urea electrolysis at large current densities, ACS Sustain. Chem. Eng. 8 (2020) 7463–7471.
[34] P. Babar, A. Lokhande, V. Karade, B. Pawar, M.G. Gang, S. Pawar, J.H. Kim, Bifunctional 2D electrocatalysts of transition metal hydroxide nanosheet arrays for water splitting and urea electrolysis, ACS Sustain. Chem. Eng. 7 (2019) 10035–10043.
[35] J.H. Yang, X. Song, X. Zhao, Y. Wang, Y. Yang, L. Gao, Nickel phosphate materials regulated by doping cobalt for urea and methanol electro-oxidation, Int. J. Hydrogen Energy 44 (2019) 16305–16314.
[36] Y. Cao, T. Wang, X. Li, L. Zhang, Y. Luo, F. Zhang, A.M. Asiri, J. Hu, Q. Liu, X. Sun, A hierarchical CuO@NiCo layered double hydroxide core-shell nanoarray as an efficient electrocatalyst for the oxygen evolution reaction, Inorg. Chem. Front. 8 (2021) 3049–3054.
[37] F. Guo, K. Ye, K. Cheng, G. Wang, D. Cao, Preparation of nickel nanowire arrays electrode for urea electro-oxidation in alkaline medium, J. Power Sources 278 (2015) 562–568.
[38] D. Liu, T. Liu, L. Zhang, F. Qu, G. Du, A.M. Asiri, X. Sun, High-performance urea electrolysis towards less energy-intensive electrochemical hydrogen production using a bifunctional catalyst electrode, J. Mater. Chem. A 5 (2017) 3208–3213.
[39] L. Xia, Y. Liao, Y. Qing, H. Xu, Z. Gao, W. Li, Y. Wu, In situ growth of porous ultrathin $Ni(OH)_2$ nanostructures on nickel foam: an efficient and durable catalysts for urea electrolysis, ACS Appl. Energy Mater. 3 (2020) 2996–3004.
[40] R.A. Hussain, I. Hussain, Fabrication and applications of nickel selenide, J. Solid State Chem. 277 (2019) 316–328.

[41] H. Liu, Z. Liu, F. Wang, L. Feng, Efficient catalysis of N doped NiS/NiS_2 heterogeneous structure, Chem. Eng. J. 397 (2020) 125507.
[42] Y. Chen, Z. Ren, H. Fu, X. Zhang, G. Tian, H. Fu, NiSe-$Ni_{0.85}Se$ heterostructure nanoflake arrays on carbon paper as efficient electrocatalysts for overall water splitting, Small 14 (2018) 1800763.
[43] Z. Liu, C. Zhang, H. Liu, L. Feng, Efficient synergism of $NiSe_2$ nanoparticle/NiO nanosheet for energy-relevant water and urea electrocatalysis, Appl. Catal. B: Environ. 276 (2020) 119165.
[44] Z. Pu, Y. Luo, A.M. Asiri, X. Sun, Efficient electrochemical water splitting catalyzed by electrodeposited nickel diselenide nanoparticles based film, ACS Appl. Mater. Interfaces 8 (2016) 4718–4723.
[45] X. Ou, J. Li, F. Zheng, P. Wu, Q. Pan, X. Xiong, C. Yang, M. Liu, In situ X-ray diffraction characterization of $NiSe_2$ as a promising anode material for sodium ion batteries, J. Power Sources 343 (2017) 483–491.
[46] Y. Bao, M. Zha, P. Sun, G. Hu, L. Feng, PdNi/N-doped graphene aerogel with over wide potential activity for formic acid electrooxidation, J. Energy Chem. 59 (2021) 748–754.
[47] H. Zhang, Y. Liu, T. Chen, J. Zhang, J. Zhang, X.W. Lou, Unveiling the activity origin of electrocatalytic oxygen evolution over isolated Ni atoms supported on a N-doped carbon matrix, Adv. Mater. 31 (2019) 1904548.
[48] S. Liu, D. Li, G. Zhang, D. Sun, J. Zhou, H. Song, Two-dimensional $NiSe_2$/N-rich carbon nanocomposites derived from Ni-hexamine frameworks for superb Na-ion storage, ACS Appl. Mater. Interfaces 10 (2018) 34193–34201.
[49] X. Li, G.Q. Han, Y.R. Liu, B. Dong, W.H. Hu, X. Shang, Y.M. Chai, C.G. Liu, NiSe@NiOOH core-shell hyacinth-like nanostructures on nickel foam synthesized by in situ electrochemical oxidation as an efficient electrocatalyst for the oxygen evolution reaction, ACS Appl. Mater. Interfaces 8 (2016) 20057–20066.
[50] J. Jia, L. Zhao, Y. Chang, M. Jia, Z. Wen, Understanding the growth of NiSe nanoparticles on reduced graphene oxide as efficient electrocatalysts for methanol oxidation reaction, Ceram. Int. 46 (2020) 10023–10028.
[51] J. Li, Z. Luo, F. He, Y. Zuo, C. Zhang, J. Liu, X. Yu, R. Du, T. Zhang, M.F. Infante-Carrió, P. Tang, J. Arbiol, J. Llorca, A. Cabot, Colloidal Ni-Co-Sn nanoparticles as efficient electrocatalysts for the methanol oxidation reaction, J. Mater. Chem. A 6 (2018) 22915–22924.
[52] X. Guo, T. Liang, D. Zhang, M. Zhang, Y. Lin, C. Lai, Facile fabrication of 3D porous nickel networks for electro-oxidation of methanol and ethanol in alkaline medium, Mater. Chem. Phys. 221 (2019) 390–396.
[53] R.M. Abdel Hameed, R.M. El-Sherif, Microwave irradiated nickel nanoparticles on vulcan XC-72R carbon black for methanol oxidation reaction in KOH solution, Appl. Catal. B Environ. 162 (2015) 217–226.
[54] M.S. Wu, G.W. Lin, R.S. Yang, Hydrothermal growth of vertically-aligned ordered mesoporous nickel oxide nanosheets on three-dimensional nickel framework for electrocatalytic oxidation of urea in alkaline medium, J. Power Sources 272 (2014) 711–718.
[55] D. Wei, W. Tang, N. Ma, Y. Wang, NiCo bimetal organic frames derived well-matched electrocatalyst pair for highly efficient overall urea solution electrolysis, J. Alloy. Compd. 874 (2021) 159945.
[56] J. Li, C. Yao, X. Kong, Z. Li, M. Jiang, F. Zhang, X. Lei, Boosting hydrogen production by electrooxidation of urea over 3D hierarchical Ni_4N/Cu_3N nanotube arrays, ACS Sustain. Chem. Eng. 7 (2019) 13278–13285.
[57] Q. Zhang, F.M.D. Kazim, S. Ma, K. Qu, M. Li, Y. Wang, H. Hu, W. Cai, Z. Yang, Nitrogen dopants in nickel nanoparticles embedded carbon nanotubes promote overall urea oxidation, Appl. Catal. B: Environ. 280 (2021) 119436.
[58] L. Zhao, Y. Chang, M. Jia, J. Jia, Z. Wen, Monodisperse $Ni_{0.85}Se$ nanocrystals on rGO for high-performance urea electrooxidation, J. Alloy. Compd. 852 (2021) 156751.
[59] J. Cao, H. Li, R. Zhu, L. Ma, K. Zhou, Q. Wei, F. Luo, Improved hydrogen generation via a urea-assisted method over 3D hierarchical NiMo-based composite microrod arrays, J. Alloy. Compd. 844 (2020) 155382.
[60] Q. Liu, L. Xie, F. Qu, Z. Liu, G. Du, A.M. Asiri, X. Sun, A porous Ni_3N nanosheet array as a high-performance non-noble-metal catalyst for urea-assisted electrochemical hydrogen production, Inorg. Chem. Front. 4 (2017) 1120–1124.
[61] C. Tang, N. Cheng, Z. Pu, W. Xing, X. Sun, NiSe nanowire film supported on nickel foam: an efficient and stable 3D bifunctional electrode for full water splitting, Angew. Chem. Int. Ed. 54 (2015) 9351–9355.